Characterization of the Creep Deformation and Rupture Behavior of DS GTD-111 Using the Kachanov–Rabotnov Constitutive Model

Calvin M. Stewart
e-mail: calvin.stewart@knights.ucf.edu

Ali P. Gordon

Department of Mechanical, Materials, and Aerospace Engineering,
University of Central Florida,
Orlando, FL 32816-2450

Erik A. Hogan
Department of Mechanical Engineering,
University of Colorado at Boulder,
Boulder, CO 80309

Ashok Saxena
College of Engineering,
University of Arkansas,
Fayetteville, AR 72701

Creep deformation and rupture experiments are conducted on samples of the Ni-base superalloy directionally solidified GTD-111 tested at temperatures between 649°C and 982°C and two orientations (longitudinally and transversely oriented). The secondary creep constants are analytically determined from creep deformation experiments. The classical Kachanov–Rabotnov model for tertiary creep damage is implemented in a general-purpose finite element analysis (FEA) software. The simulated annealing optimization routine is utilized in conjunction with the FEA implementation to determine the creep damage constants. A comparison of FEA and creep deformation data demonstrates high accuracy. Using regression analysis, the creep constants are characterized for temperature dependence. A rupture prediction model derived from creep damage evolution is compared with rupture experiments. [DOI: 10.1115/1.4003111]

Keywords: creep, material modeling, constitutive modeling, creep damage, directionally solidified, DS GTD-111, temperature dependence, life prediction, tertiary

1 Introduction

The advent of directionally solidified (DS) superalloys has led to major advancements in the power generation industry where components experience high load and temperature environments [1]. Directional solidification involves the casting of a material so that grain boundaries are aligned at a desired orientation. During casting, a columnar-grained structure is achieved by controlled withdrawal of a water cooled mold from the hot zone of a furnace. Induction heating methods provide an adequate thermal gradient that prevents nonuniformities due to solidification in advance of the liquid-solid interface [2]. The results of casting are long grains, which enhanced impact strength, stiffness, high temperature creep, and fatigue resistance and improved corrosion resistance, while intergranular cracking was inhibited in transverse (T) orientations.

Current industry material modeling techniques can be improved via application of more accurate constitutive models. Common practice in the estimate of high temperature deformation couples a secondary creep modeling with a plasticity model in a finite element software package. Secondary creep modeling alone is not enough. In some cases, service conditions are such that the tertiary creep regime is unavoidable. This is particularly important for components under high load and temperature where the tertiary creep regime can quickly and unexpectedly initiate. It is important to include tertiary creep modeling because it allows an engineer to determine the secondary-tertiary creep transition time and to remove components from service before rapid nonlinear tertiary creep deformation occurs.

Another fault in current modeling techniques is the typical neglect of temperature dependence. This prevents the modeling of quasi-static thermal cycling and can lead to a misestimation of the creep strain as the structure experiences variable thermal loading.

In this paper, a tertiary creep damage model has been implemented to improve the prediction of creep deformation and rupture of DS GTD-111, a Ni-base superalloy. Secondary creep constants are analytically determined based on experiments from literature [3]. A creep rupture time model is derived and utilized to determine initial tertiary creep constants. Creep deformation and rupture experiments are used in conjunction with an advanced optimization routine to determine the optimal tertiary constants at each orientation and multiple temperatures. The secondary and tertiary creep constants are written into a temperature-dependent form. Predictions of critical damage and rupture time are provided and compared with experimental data.

2 Directionally Solidified GTD-111

The subject material superalloy DS GTD-111, a dual-phase Ni-base superalloy, was developed in 1987 as a first stage bucket material from uniaxial GTD-111 (derived from René 80 [4]). Directionally solidified GTD-111 is commonly used in gas turbine applications [5]. General Electric uses the material on the first stage in MS7F/MS9F, MS3002, and MS5002C units [6]. The structure of the grains has been found to produce enhanced creep life, impact strength, corrosion, and thermal fatigue resistance compared with its equiaxed counterpart [1,7–9]. The material is transversely isotropic in the x_1-x_2 plane, while different material properties are found on the x_3 normal plane (Fig. 1).

During casting, a columnar-grained structure is achieved by controlled withdrawal of a water cooled mold from the hot zone of a furnace. Induction heating methods provide an adequate thermal gradient that prevents nonuniformities due to solidification in advance of the liquid-solid interface [2]. The long grains inhibit intergranular cracking in the x_1-x_2 orientations, the major cause of failure in turbine blades. These long grains reduce the Young's modulus in the longitudinal (L) orientation, resulting in increased elastic strain and reduced thermal stresses. A consequence of long

Contributed by the Materials Division of ASME for publication in the JOURNAL OF ENGINEERING MATERIALS AND TECHNOLOGY. Manuscript received June 11, 2010; final manuscript received September 1, 2010; published online March 21, 2011. Editor: Hussein Zbib.

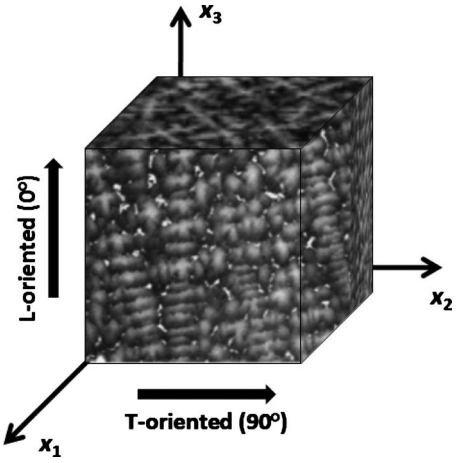

Fig. 1 Grain structure of DS GTD-111 with microstructure imposed

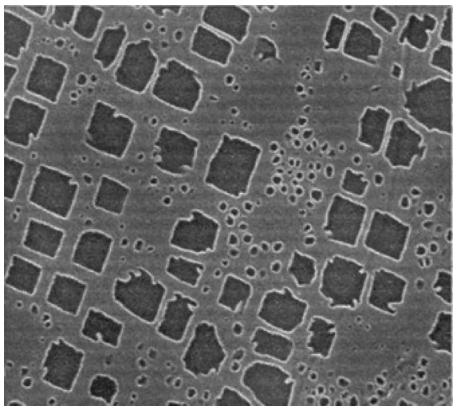

Fig. 3 Dark areas are the bimodal γ' precipitated particles

columnar grains is that the L orientation exhibits enhanced strength, ductility, and time before rupture compared with equiaxial polycrystalline (PC) GTD-111.

Through optical and scanning electron microscopy investigations, a closer look at the grain structure of the material was resolved. Figure 2 shows the grain structure of both L and T orientations. The direction of solidification is the x_1-x_2 plane; thus, the individual grains' ends can be observed in this orientation. The long grains can be observed on both x_2-x_3 and x_1-x_3 planes with some slight nonuniformity in orientation. Tighter control of the thermal gradient could produce improved grain direction uniformity.

The nominal chemical composition of DS GTD-111 in wt % is given in Table 1. Microstructurally, DS GTD-111 contains a nickel austenite (γ) matrix, bimodally distributed gamma prime (γ') precipitated particles, γ-γ' eutectic, carbides, and small amounts of topological close-packed phases σ, δ, η, etc., as observed in Fig. 3 [8,10]. It has a high volume fraction of gamma prime (γ') precipitated particles (approximately 60%), which imparts enhanced impact strength, high temperature creep and fatigue resistance, and improved corrosion resistance. In the case of PC GTD-111, to obtain the desired microstructure, heat treatment is used and then abruptly interrupted, leading to a γ-γ' microstructure that is metastable. Polycrystalline GTD-111 contains 0.86 μm and 0.1 μm primary and secondary precipitated particles, respectively. The γ' precipitated particles can morph (shape, arrangement, size, etc.) to decrease the local energy state of the lattice [11]. In the case of DS GTD-111, the microstructure is formed at the liquid-solid interface, and slow cooling during processing produces large grains, 0.5 μm width primary cooling γ' precipitated particles, and 0.05 μm width secondary cooling γ' precipitated particles. The average grain size is $5\times5\times125$ mm^3 [12]. Components with this microstructure can be challenging to repair if extensively damaged; however, a number of methods are under investigation to mitigate this problem [4,9].

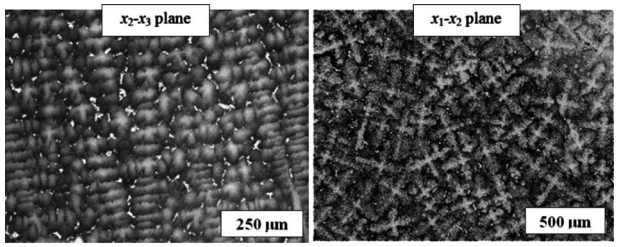

(*a*) (*b*)

Fig. 2 Grain structure of GTD-111: (*a*) T-oriented specimen and (*b*) L-oriented specimen

3 Creep Test Data

Creep deformation and rupture experiments were conducted on L- and T-oriented specimens of DS GTD-111 according to an ASTM standard E-139 [13] at temperatures ranging from 649°C to 982°C and various uniaxial tensile stress levels to determine the creep response of the material over a wide range of conditions. A list of all creep deformation and rupture test data used is provided in Table 2 [10]. The 0.2% yield strength, ultimate tensile strength (UTS), and estimated primary creep strain are listed as well. The estimated primary creep strain is the strain at which the minimum creep strain rate is reached. From experiments, it is observed that primary creep strain has a very limited effect on rupture strain and time.

The onset of creep occurs at 0.4–0.6 T_m, the melting temperature. At 649°C, creep deformation is minimal; therefore, the experiment at 649°C and 896 MPa is set slightly above the yield strength and exhibits some limited plasticity. The 649°C experiment was used to set a lower temperature bound for the creep behavior. For all cases, except those at 649°C, time-independent plasticity is ignored. Generally, creep rupture time increases with either decreasing applied stress or decreasing temperature. Specimens were obtained from three batches of DS GTD-111, where each batch exhibited a slightly different creep response. In all the creep rupture data, scatter is present. This form of scatter, which is common in creep rupture data, is due to random inconsistencies in the microstructure or inadequate control of the heat treatment process. Manufacturers commonly use a least-squares linear regression analysis to determine the minimum creep rupture life of an

Table 1 Nominal chemical composition (wt %) of DS GTD-111 superalloy [6]

Element	Cr	Co	Al	Ti	W	Mo	Ta	C	Zr	B	Fe	Si	Mn	Cu	P	S	Ni
Min	13.7	9.0	2.8	4.7	3.5	1.4	2.5	0.08	0.005	–	–	–	–	–	–	–	Bal.
Max	14.3	10.0	3.2	5.1	4.1	1.7	3.1	0.12	0.040	0.020	0.35	0.3	0.1	0.1	0.015	0.005	Bal.

Table 2 Creep deformation, rupture data, and least-squares values for DS GTD-111 [10]

Matl. orient. α (deg)	Temperature °C	Temperature °F	Stress MPa	Stress ksi	0.2% yield strength (MPa)	Ultimate tensile strength (MPa)	Rupture strain (%)	Rupture tim e(h)	Estimated primary creep (%)	Least-squares value
L (0)[a]	649	1200	896	130	825	1110	4.9	465.9	0.13	2.0588
L (0)[a]	760	1400	408	60	903	1108	15.0	5624.0	0.30	9.6451
L (0)	760	1400	613	89	903	1108	13.2	243.6	0.24	1.6003
T (90)	760	1400	517	75	776	974	6.9	375.7	0.60	9.029
T (90)	760	1400	613	89	776	974	1.8	42.6	0.36	9.2964
L (0)	816	1500	455	66	787	991	21.5	321.5	0.26	0.4058
T (90)	816	1500	455	66	720	932	4.6	127.0	0.21	2.9972
L (0)	871	1600	241	35	669	802	18.8	2149.0	NA	3.7922
L (0)	871	1600	289	42	669	802	11.7	672.2	0.09	4.1546
T (90)	871	1600	241	35	666	834	7.6	980.2	NA	8.3388
T (90)	871	1600	289	42	666	834	5.1	635.3	NA	4.2331
L (0)	940	1724	244	35	NA	458	14.1	68.7	0.07	0.8296
T (90)[a]	940	1724	244	35	NA	626	3.8	62.5	0.07	7.7568
L (0)	982	1800	124	18	NA	191	17.8	821.3	0.01	5.7186
L (0)	982	1800	145	21	NA	191	9.1	301.7	NA	0.6798

[a]Manually fit.

alloy while neglecting scatter. Advancements by Zuo et al. [14] show that the maximum likelihood method produces more accurate predictions of creep rupture life.

From the creep deformation and rupture experiments, the subject material DS GTD-111 exhibits primary, secondary, and tertiary creep strains depending on the combination of test temperature and stress, and material orientation. Based on these strain responses, the deformation mechanisms can be inferred from investigations that complemented mechanical experimentation with a microscopic analysis. In all cases, primary creep has limited influence on rupture strain and time. Deformation at 649°C at high stresses is mostly due to elastic strain, along with a limited primary creep and a majority secondary creep. At higher temperatures (760°C and above), deformation is dominated by secondary and tertiary creep facilitated by the coalescence of grain boundary voids into microcracks.

4 Secondary Creep Constants

In order for the tertiary creep damage model to correctly predict creep deformation up to rupture, the secondary creep constants for DS GTD-111 need to be determined. Earlier work shows that the classical Norton creep power law works well in predicting the steady-state strain found in the secondary regime. The Norton power law for secondary creep is as follows:

$$\dot{\varepsilon}_{\mathrm{cr}} = A\bar{\sigma}^n \tag{1}$$

where A and n are the creep strain coefficient and exponent, respectively, and $\bar{\sigma}$ is the von Mises effective stress. Simple analytical methods can be used to determine the secondary creep constants A and n at various temperatures [15]. These analytical methods, although good, require duplication of creep tests and then averaging to eliminate scatter. In the case of this study, limited test data are available; thus, a numerical approach is used. The minimum creep strain rate and the specimen stress load are put into the Norton power law, and a system solving algorithm is used to determine optimal A and n constants. For most materials, traditional methods tend to find A and n to be stress independent, but there are exceptions [16]. Hyde et al. [17] showed for a Ni-base alloy, Waspaloy, that once a critical value of applied stress is reached the relationship between minimum creep strain and stress evolves. This leads to a two-stage relationship and stress dependence of the secondary material constants. Sajjadi and Nategh [8] showed that for equiaxial GTD-111 there is an abrupt shift in deformation mechanism at intermediate temperature and stress levels, which causes a breakdown of power law creep. Table 2 shows that for the collected creep deformation data, at the maximum, two stress levels per temperature were conducted. Any possible stress dependence of A and n is not visible in the present data; therefore, stress dependence of the secondary material constants is neglected.

Dorn [18] suggested that temperature dependence should take the form of an Arrhenius equation,

$$A(T) = B\exp\left(\frac{-Q_{\mathrm{cr}}}{RT}\right) \tag{2}$$

where B is the pre-exponential factor in $\mathrm{MPa}^{-1}\,\mathrm{h}^{-1}$, Q_{cr} is the activation energy for creep deformation in J mol^{-1}, R is the universal gas constant 8.314 J mol^{-1} K, and T is the temperature in kelvin. Jeong et al. [19] demonstrated that while under stress relaxation, short term transient behavior occurs, where Q_{cr} and n are both stress dependent at relativity short times (e.g., less than 10 min). After this transient stage, the Norton power law becomes independent of initial stress and strain. This transient behavior has been neglected here since the present study focuses on longer periods (e.g., 1–100,000 h). For DS GTD-111, the activation energies for creep deformation, Q_{cr}, have been found to be 3773 kJ/mol and 3636 kJ/mol. These values are much higher than the activation energy of self-diffusion for equiaxial PC GTD-111 and other polycrystalline Ni-base superalloys [8,20]. Ibanez suggested that dislocation climbing is not a viable creep mechanism for DS GTD-111 [3]. The larger activation energy is a result of creep controlled dislocation motion, a common occurrence in multiphase superalloys. Previously, efforts to model the secondary creep constants for DS GTD-111 were not easily fittable into a temperature-dependent form [10]. The temperature dependence of A and n in this study is proposed as

$$A(T) = A_0\exp(A_1 T) \tag{3}$$

$$n(T) = n_1 T + n_0 \tag{4}$$

where A_0, A_1, n_0, and n_1 are constants and T is in °C. A plot of these functions in Fig. 4 shows accurate predictions ($R^2 > 0.9672$). Using these formulations, the temperature dependence of secondary creep can be modeled.

5 Constitutive Model

A constitutive model that can account for both secondary and tertiary creep regimes must be developed. In the present study, the development of a primary creep model is not necessarily due to the minimal amount of primary creep strain recorded during creep tests. The relatively short regime is approximated by a static pri-

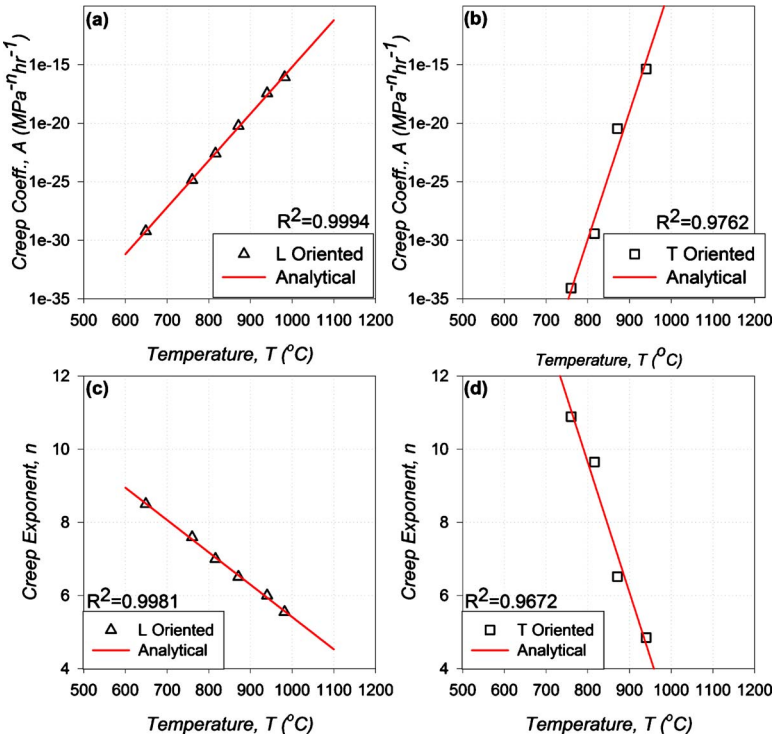

Fig. 4 Secondary creep constants for DS GTD-111

mary creep strain applied upon loading. The Norton power law is used to account for steady-state creep in the form

$$\dot{\varepsilon}_{\mathrm{cr}} = \frac{d\varepsilon_{\mathrm{cr}}}{dt} = A\bar{\sigma}^n \tag{5}$$

where A and n are the creep strain coefficient and exponent, and $\bar{\sigma}$ is the von Mises effective stress.

To account for tertiary creep, a continuum damage mechanics model was applied. This involves the use of a damage variable, which accounts for microstructural evolution. During the transition from secondary to tertiary creep, microcracks along grain boundaries of polycrystalline materials act as stress concentrations. The amplified stress due to local reduction in cross-sectional area is the phenomenological basis of the damage variable, ω, that is coupled with the creep strain rate and has a stress-dependent evolution, i.e.,

$$\dot{\varepsilon}_{\mathrm{cr}} = \dot{\varepsilon}_{\mathrm{cr}}(\bar{\sigma}, T, \omega, \ldots)$$

$$\dot{\omega} = \dot{\omega}(\bar{\sigma}, T, \omega, \ldots) \tag{6}$$

A straightforward formulation implies that the damage variable is the net reduction in cross-sectional area due to the presence of defects such as voids and/or cracks, e.g.,

$$\bar{\sigma}_{\mathrm{net}} = \bar{\sigma}\frac{A_0}{A_{\mathrm{net}}} = \frac{\bar{\sigma}}{\left(1 - \dfrac{A_0 - A_{\mathrm{net}}}{A_0}\right)} = \frac{\bar{\sigma}}{(1-\omega)} \tag{7}$$

where $\bar{\sigma}_{\mathrm{net}}$ is referred to as the net (area reduction) stress, A_0 is the undeformed area, A_{net} is the reduced area due to deformation, and ω is the damage variable. Some models account for the variety of physically observed creep damage mechanisms with multiple damage variables [21]. An essential feature of damage required for the application of continuum damage mechanics concepts is a continuous distribution of damage. Generally, microdefect interaction (in terms of stress fields, strain fields, and driving forces) is relatively weak until impingement or coalescence is imminent.

The damage variable is applied in a first-order differential equation for the damage evolution and coupled with the creep strain rate. Work by Kachanov [22] and, later, by Rabotnov [23] led to the coupled Kachanov–Rabotnov equations of creep,

$$\dot{\varepsilon}_{\mathrm{cr}} = \frac{d\varepsilon_{\mathrm{cr}}}{dt} = A\left(\frac{\bar{\sigma}}{1-\omega}\right)^n \tag{8}$$

$$\dot{\omega} = \frac{d\omega}{dt} = \frac{M\bar{\sigma}^{\chi}}{(1-\omega)^{\phi}} \tag{9}$$

where the coefficients A and M and the exponents n, χ, and ϕ are damage constants. Johnson et al. [24] showed the importance of modeling beyond simple uniaxial tension conditions and focused on multi-axial states of stress. A model that can implement complex states of stress is necessary to accurately model gas turbine components. Tensile/compressive asymmetry and multi-axial behavior can be accounted for by using the damage evolution equation developed by Hayhurst [25], i.e.,

$$\dot{\omega} = \frac{d\omega}{dt} = \frac{M\sigma_r^{\chi}}{(1-\omega)^{\phi}} \tag{10}$$

$$\sigma_r = \langle \alpha\sigma_1 + 3\beta\sigma_m + (1-\alpha-\beta)\bar{\sigma} \rangle \tag{11}$$

where the von Mises stress $\bar{\sigma}$ is replaced by the Hayhurst triaxial stress σ_r. The Hayhurst triaxial stress is related to the principal stress σ_1, the hydrostatic (mean) stress σ_m, and the von Mises effective stress $\bar{\sigma}$, and it includes two weight factors, α and β, that are determined from multi-axial creep experiments. The Hayhurst triaxial stress becomes incompressible when $\alpha+2\beta \geq 1$. More recent investigations have extended this damage evolution description to account for anisotropic damage of isotropic materials resulting from multi-axial states of stress [26,27]. In these cases, damage is described by a second-rank tensor.

Using Eqs. (8), (10), and (11), a suitable tertiary creep damage model is resolved. The tertiary creep damage model can be re-

verted back to secondary creep when $M=0$. Damage evolution becomes zero, and the strain rate reverts back to the Norton power law for secondary creep, with the exception that $\bar{\sigma}$ is replaced by σ_r. This is a useful property that has been exploited in a previous study to determine the transition time when the dominant creep regime shifts from secondary to tertiary creep [20].

The tertiary creep damage model has been used in a variety of studies of turbine and rotor materials. The constants A, n, M, χ, and ϕ are considered material properties. Stewart and Gordon showed that by determining the creep material constants at multiple temperatures for Ni-base alloy IN-617, functions that introduce temperature dependence to the tertiary creep damage model can be developed [20]. This has the effect of making the creep strain rate and damage evolution equations temperature dependent. As temperature changes over time, the material constants change, altering the creep strain rate and damage evolution predicted at the current time step.

6 Rupture Prediction Model

A prediction of the rupture time can be achieved using the damage evolution formulation (Eq. (10)). Integration of the equation leads to the following:

$$(1-\omega)^{\phi} d\omega = M\sigma_r^{\chi} dt$$

$$-\frac{(1-\omega)^{\phi}}{1+\phi}\Bigg|_{\omega_o}^{\omega} = M\sigma_r^{\chi}\big|_{t_o}^{t} \tag{12}$$

where under creep experiment conditions, stress is constant and t_o and ω_o are equal to 0.0. Simplification leads to the rupture time and damage predictions,

$$t = [1-(1-\omega)^{\phi+1}][(\phi+1)M\sigma_r^{\chi}]^{-1} \tag{13}$$

$$\omega(t) = 1-[1-(\phi+1)M\sigma_r^{\chi}t]^{1/(\phi+1)} \tag{14}$$

When adequate damage constants are determined, a high-caliber prediction of rupture time can be achieved. Plotting stress versus rupture time on a log scale produces a linear relationship similar to what is observed for brittle failure of other PC Ni-base superalloys [28]; however, under short life and high stress conditions (particularly near the ultimate tensile strength), the rupture time predictions deteriorate. This is due to the formulation not directly including the effects of the ultimate tensile strength in damage evolution. Applying it would provide a criterion by which the model could converge to the instantaneous failure when loaded beyond the ultimate tensile strength. Under actual service conditions, components are typically under significantly less stress and designed for longer life than the typical creep test. Secondary creep is dominant, and the rupture time equation is quite useful in predicting failure. Additionally, the rupture time equation can be applied to determine an initial guess set of damage constants. This can be done through optimization when it is assumed that $\omega(t)$ equals 1.0 at the experimental rupture time, t_r.

7 Numerical Approach

The constitutive model described in Eqs. (8), (10), and (11) has been implemented in a general-purpose finite element analysis (FEA) software in order to determine the constants for the constitutive model used in the secondary-tertiary creep formulation. The formulation was implemented into a FORTRAN subroutine in the form of a user-programmable feature (UPF) in ANSYS. The subroutine is incorporated with an implicit integration algorithm. This backward Euler integration algorithm is more accurate over long time periods than other practical numerical integration methods. This allows larger time steps that reduce the numerical solve time. Since the viscoplastic/creep behavior of materials is significant at extended histories, the backward Euler method is the desired method for the integration of creep constitutive models [29].

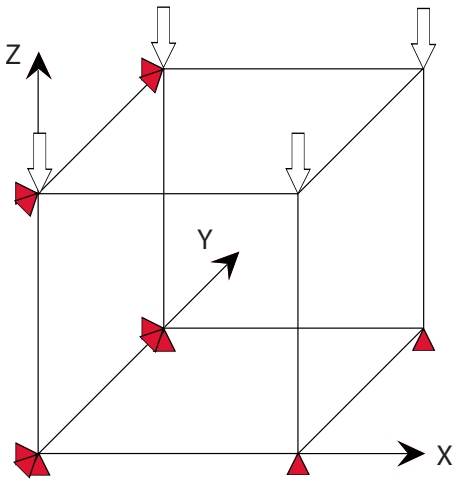

Fig. 5 Single element FEM geometry used with force and displacement applied

This implementation allows for the update of the internal state variable, ω. Initially, ω equals 0.0, and during loading, ω increases. To prevent the singularity that is caused by rupture (e.g., ω equals 1.0), the damage is restricted to a maximum of 0.90. A comparison of creep rupture data to numerical simulations shows that rupture occurs at ω between 0.4 and 0.6; therefore, rupture can be achieved before a singularity occurs. To prevent an excessive model solve time and large deformation errors, a simulation was terminated once the total strain reached 100%. If needed, this model can be applied with time-independent and time-dependent plasticity models in a straightforward manner.

The UPF has been used to simulate the temperature and stress loading conditions of a series of uniaxial creep and rupture experiments. A single, solid, three-dimensional, eight-noded element was used, and the appropriate initial and boundary conditions were applied to numerically simulate uniaxial creep tests. The loads and temperatures applied numerically simulated those of the obtained creep rupture experiments. Figure 5 demonstrates how these conditions are applied on the finite element model (FEM) geometry. The constant axial load experience during creep testing was applied on the top surface of the element. A uniform temperature was applied. Displacement controls were set to match the constraints experienced during the simulation. These conditions lead to an accurate assessment of the creep deformation within a single element model. Histories of creep deformation, $\varepsilon_{cr}(t)$, were recorded to a data file and subsequently compared with experiments. Using this method, expansion beyond a single element to multi-element simulations will produce an accurate measure of creep deformation.

8 Optimization

To determine the creep damage parameters M, χ, and ϕ, an automated optimization routine, called USHARP [30], was used. FEM simulations were carried out and compared with their corresponding experimental data sets. In each case, the stress and temperature specified in the ANSYS simulation matched those of the corresponding experimental data set. ANSYS simulations were then executed in an iterative optimization process until the least-squares values between the simulated and experimental data sets were minimized. The least-squares objective function was based on creep strain and is presented as

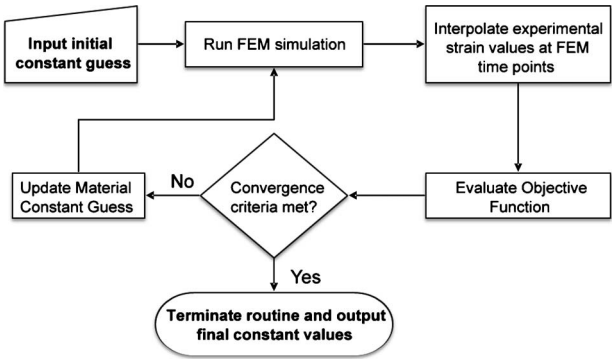

Fig. 6 USHARP optimization framework [30]

$$S = \frac{\sum_{i=1}^{m} (\varepsilon_{\mathrm{FEM},i} - \varepsilon_{\mathrm{expt},i})^2}{m} \tag{15}$$

where $\varepsilon_{\mathrm{FEM},i}$ and $\varepsilon_{\mathrm{expt},i}$ are the strain values obtained by FEM simulation and experimental testing, respectively. The parameter m is the total number of data points resulting from an individual simulation used to determine the least-squares value during a single iteration. In Eq. (15), the objective function assumes that the strains correspond to an identical load time. Since the cardinality of the data sets always differed, an automated smoothing routine was carefully developed to unify the time basis of the data. This feature is built into USHARP.

The simulated annealing multimodal algorithm was used as the optimization algorithm [31]. It is a robust optimizer, which has the capability to find the global optimal by both uphill and downhill moves. This capability allows it to effectively climb out of local minima when necessary. Additionally, its implementation into the USHARP routine was very straightforward [32]. The USHARP code automatically executes ANSYS at each iteration, evaluates the objective function, and updates the guess for the material constants on the basis of the simulated annealing algorithm. An overview of the optimization procedure is provided in Fig. 6.

Due to simulated annealing being a nonconventional algorithm, it requires an extensive number of iterations before final convergence to the global optima occurs. To reduce solve time, the solve space or target range to be optimized needed to be determined. To do this, the lowest and highest temperature experiments were conducted first. The solve space was set such that the lower and upper bounds for all three damage constants were $\pm 1.0 \times 10^{10}$. The results of these simulations were analyzed, and target ranges for the intermediate temperature experiments were set as $0.0 \leq M \leq 700$, $1.7 \leq \chi \leq 2.3$, and $0.0 \leq \phi \leq 60$. The simulated annealing routine requires an initial guess. To determine a suitable set of initial constants, the derived rupture time model, Eq. (13), was compared with experimental data. Manual iteration of the M, χ, and ϕ was performed until the relative error between experimental and simulated rupture times was minimized. This produced constants that were readily applicable in the USHARP routine.

The Kachanov–Rabotnov damage evolution equations do not account for primary creep. Primary creep strain was therefore approximated from experimental data and added to the finite element solution. These modified creep strain values were applied in the least-squares calculations and were plotted with the experimental data. As a result, the secondary creep regions of each curve conferred a better fit on the tertiary creep region. This ensured that more accurate material constants were determined. The primary creep values used for each data set are presented in Table 2.

As the optimization routine progressed, the least-squares values were recorded at every iteration. This provided a clear display of convergence using the simulated annealing algorithm, as presented for every tenth iteration in Fig. 7. It is observed that simulated annealing continuously moved both up and downhill toward a minimal least-squares value. Depending on the quality of the initial guess, the number of iterations until convergence greatly varies. A least-squares value less than 10 was necessary during each optimization run. Otherwise, an improved initial guess would be selected and optimization would be performed again until a suitable value was obtained.

A list of the least-squares values found is in Table 2. In all cases, the optimization routine on average produces better least-squares values for the L orientation. This can be attributed to the slight variability in alignment of the long grains between different specimens. For a number of experimental data sets, simulated annealing was unable to determine a suitable set of constants. In these experiments, strain softening beyond the minimum creep rate was minimal. As a consequence, the creep damage parameters could not properly be optimized by USHARP. Instead, the values for the material constants were obtained manually until a suitable set of constants could be realized. Then, the least-squares formulation was applied to determine the quality of fit. Damage constants were optimized for every combination of temperature and stress.

9 Results

9.1 Creep Deformation. Optimization of the Kachanov–Rabotnov isotropic creep damage formulation to the creep test experimental data has been used to determine the tertiary creep damage constants, M, χ, and ϕ. A list of these optimized constants is presented in Table 3. For each of the available creep tests, the final optimized finite element solution has been superimposed with creep deformation data, as shown in Fig. 8. It should be noted that primary creep approximations were added directly to the collected FEM deformation data to account for the primary creep regime. It is observed that for all 16 creep tests, high-caliber fits to the creep deformation data were achieved. The isotropic creep damage model is found to accurately model the creep deformation as measured from a uniaxial specimen.

The behavior of the tertiary creep damage constants with respect to temperature is very important. Temperature-dependent functions of the tertiary creep damage constants for both L and T orientations of DS GTD-111 would allow accurate modeling of creep strain that develops in directionally solidified components under a thermal gradient. Taking the results of the optimization routine, an automated curving-fitting tool was used to determine suitable functions for the damage evolution constants. The tertiary creep damage coefficient, M, was found to work well in an exponential equation of the form

$$M(T) = \lambda_1 M_1 \exp(\lambda_2 M_0 T)$$

$$\begin{pmatrix} \mathbf{L} \\ \mathbf{T} \end{pmatrix} \text{orientation} = \begin{cases} \lambda_1 = \lambda_2 = 1 \\ \lambda_1 = 0.8245, \quad \lambda_2 = 1.0722 \end{cases} \tag{16}$$

where T is in °C and M_1 ($\mathrm{MPa}^{-\chi}\,\mathrm{h}^{-1}$) and M_0 (unitless) are constants. The unitless weight values λ_1 and λ_2 were used to implement the formulation for both L and T orientations. Ideally, the creep constants would be expressed in terms of tensile data (e.g., yield strength and UTS); however, that is saved for future study. Figure 9 shows the regression fit of the temperature-dependent function to the optimized constants. The temperature-dependent functions for the tertiary creep damage coefficient, M, carry R^2 values of 0.9593 and 0.9409 for L- and T-oriented specimens, respectively.

The tertiary creep damage exponent, χ (unitless), was found to exhibit no perceivable temperature dependence. The average values for L and T were observed as 2.1292 ± 0.2160 and 2.0994 ± 0.2834, respectively. Small changes in the χ tertiary creep damage exponent have a strong effect on the damage rate and, consequently, the M and ϕ tertiary creep damage constants.

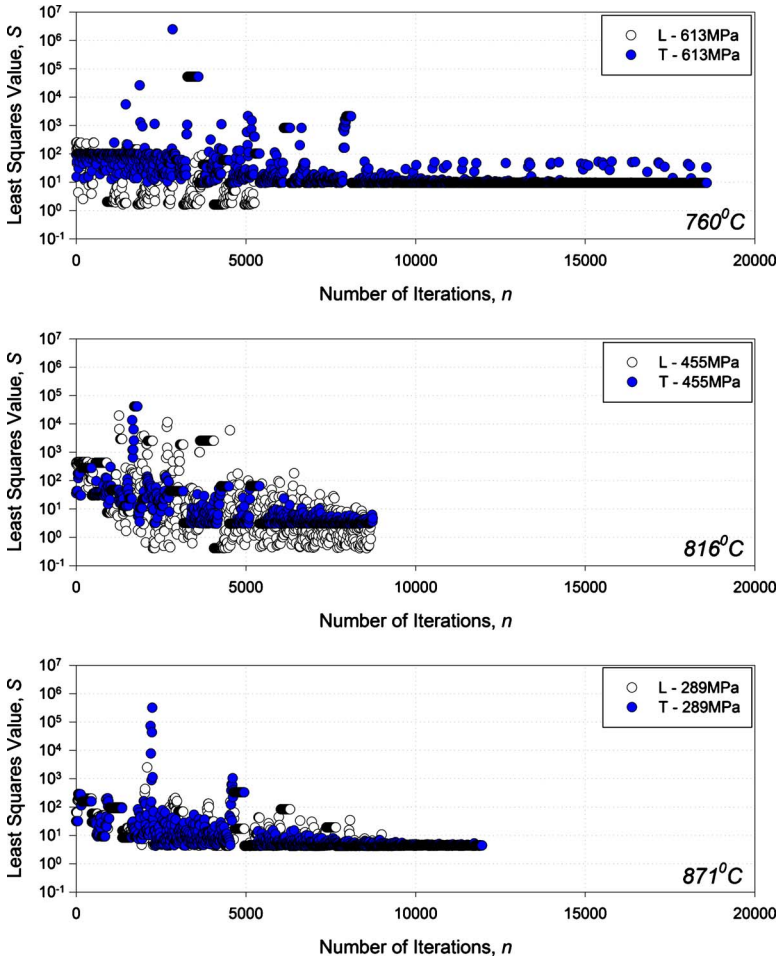

Fig. 7 Least-squares values presented for every tenth iteration during optimization

The placement of the tertiary creep damage exponent, χ, as a power of stress, σ, sets the χ constant as a stress sensitivity factor. The fluctuations in the χ tertiary creep damage constants found in the optimized fits (Table 3) have a detrimental effect on the caliber of the temperature-dependent regression fits for the M and ϕ tertiary creep damage constants.

Again, ideally, the temperature dependence of creep constants would be expressed in terms of tensile data, but this is saved for

Table 3 Tertiary creep damage constants for DS GTD-111

	Temperature		Stress		Tertiary creep damage constants			Functional fit, f(T)		
Matl. orient. α (deg)	°C	°F	MPa	ksi	M (MPa$^{-\chi}$ h^{-1})	χ	ϕ	M (MPa$^{-\chi}$ h^{-1})	χ	ϕ
L (0)	649	1200	896	130	10.000	1.880	55.000	6.009	2.129	55.093
L (0)	760	1400	408	60	20.847	1.900	8.500	28.556	2.129	10.342
L (0)	760	1400	613	89	19.784	2.231	13.261	28.556	2.129	10.342
T (90)	760	1400	517	75	36.161	2.106	14.810	50.881	2.099	29.210
T (90)	760	1400	613	89	51.801	2.203	39.931	50.881	2.099	29.210
L (0)	816	1500	455	66	64.127	2.257	3.792	62.686	2.129	6.249
T (90)	816	1500	455	66	167.590	1.981	28.224	118.221	2.099	17.444
L (0)	871	1600	241	35	96.015	2.022	7.161	135.691	2.129	7.351
L (0)	871	1600	289	42	131.010	2.054	9.698	135.691	2.129	7.351
T (90)	871	1600	241	35	263.010	2.098	2.296	270.579	2.099	9.446
T (90)	871	1600	289	42	345.840	1.919	6.823	270.579	2.099	9.446
L (0)	940	1724	244	35	579.120	2.310	7.069	357.522	2.129	8.018
T (90)	940	1724	244	35	600.000	2.290	7.069	764.588	2.099	4.396
L (0)	982	1800	124	18	655.930	2.221	3.278	644.780	2.129	4.070
L (0)	982	1800	145	21	665.200	2.288	5.126	644.780	2.129	4.070

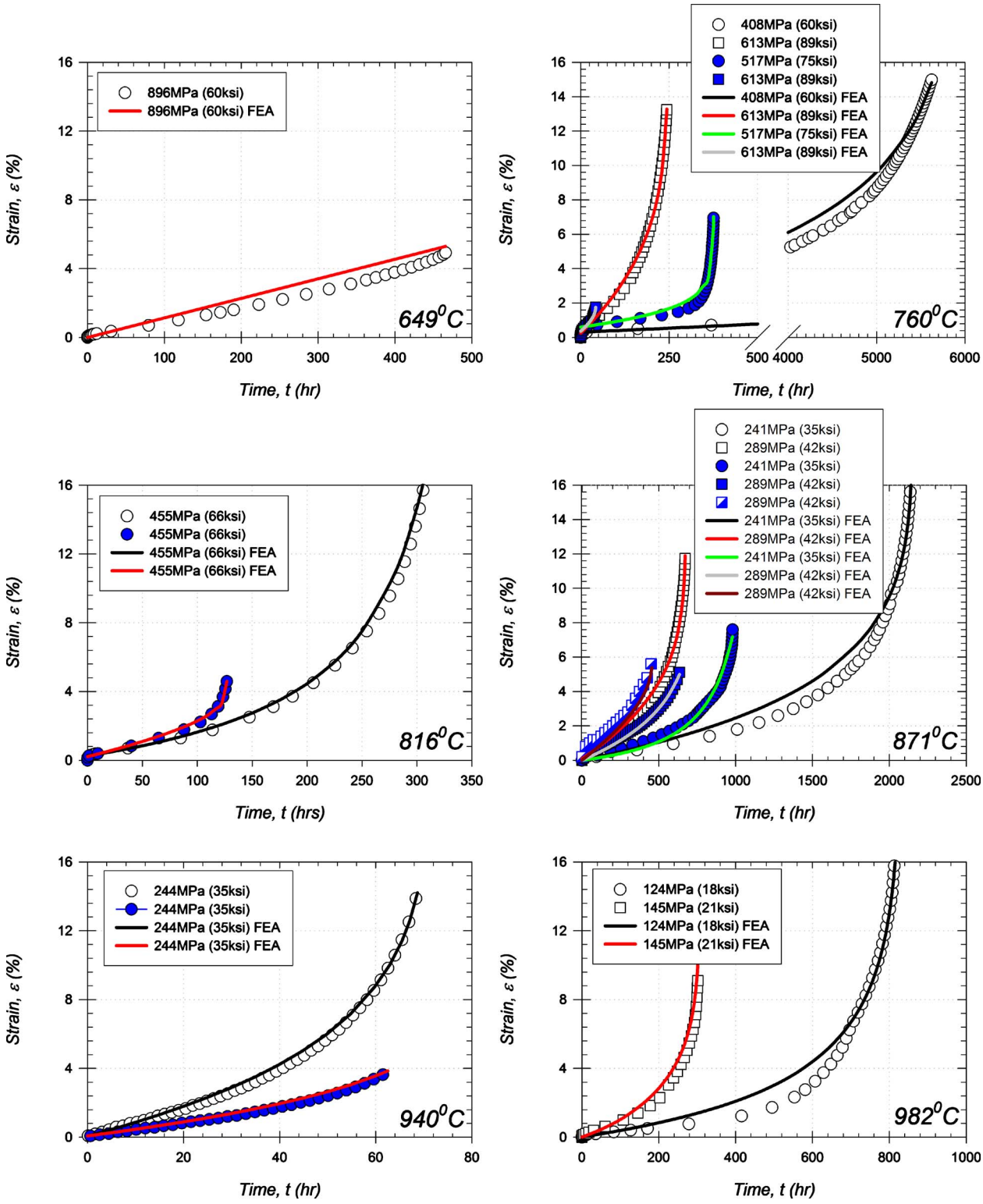

Fig. 8 Creep deformation fits of L (open) and T (filled) DS GTD-111 at temperatures of 649–982°C using the isotropic Kachanov–Rabotnov formulation

future study. In the present study, the tertiary creep damage exponent, ϕ, was found to produce a less than ideal fit to temperature in a polynomial equation of the form

$$\phi(\sigma) = \phi_3 T^3 + \phi_2 T^2 + \phi_1 T + \phi_0 \tag{17}$$

where T is in °C, and ϕ_0, ϕ_1, ϕ_2, and ϕ_3 are constants (independent sets for both L and T). Figure 10 shows the regression fit of the temperature-dependent function to the optimized constants. The temperature-dependent functions for the tertiary creep damage constants, ϕ, carry R^2 values of 0.9876 and 0.5309 for L- and T-oriented specimens, respectively. The low R^2 value in the T-oriented specimen data is likely due to the fluctuations observed in the χ tertiary creep damage constants. These slight fluctuations

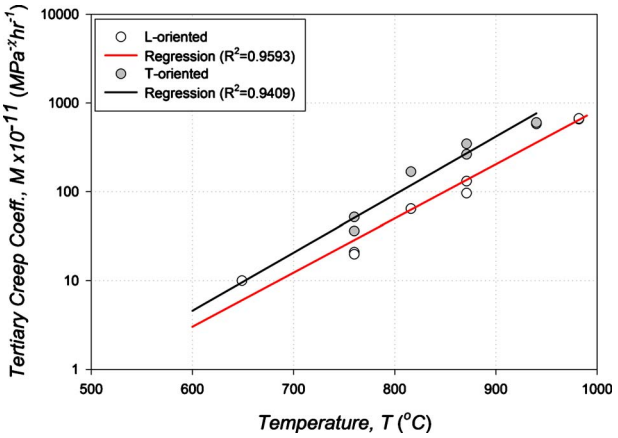

Fig. 9 Temperature dependence of the *M* tertiary creep damage constants for DS GTD-111

necessitate an observable shift in the ϕ tertiary creep damage constants to produce an accurate damage rate. This issue could be eliminated by conducting another batch optimization where the χ tertiary creep damage constants are negated as a possible temperature-dependent variable. Setting the χ tertiary creep damage constants as the known average from the initial optimization

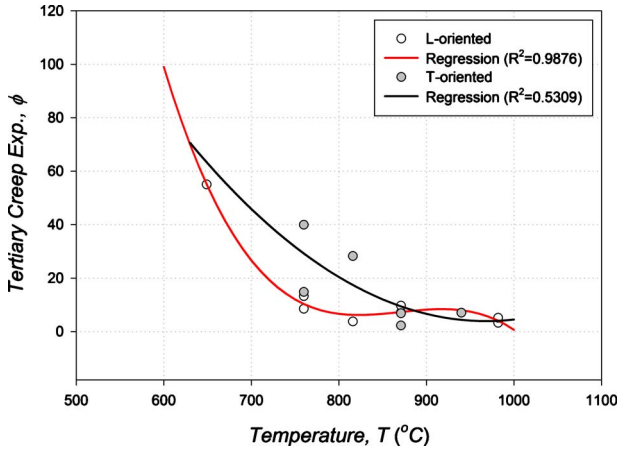

Fig. 10 Temperature dependence of the ϕ tertiary creep damage constants for DS GTD-111

could improve the modeling of the temperature dependence of the tertiary creep damage constants. Additionally, the weak dependence could be a symptom of the lower number of experimental tests available for the T orientation and/or microstructural inconsistency due to the use of three different material batches. In general, the R^2 achieved could be improved by conducting additional experiments in the L and T orientations and by removing outlier data points.

The formulation could be modified by relating the tertiary creep damage constants as a function of temperature-dependent material properties. This could be done with a quantitative analysis of the correlation between elastic and plastic material properties with the M and ϕ constants.

The implication of using these temperature-dependent functions is that it allows model structures whose boundary conditions include thermal gradients. Regions at elevated temperatures will undergo a higher level of creep deformation compared with those at lower temperatures. Using these functions leads to simulations that more accurately predict the locally critical points. Along similar lines, creep deformation during thermal cycling can be considered.

9.2 Rupture Predictions. Before analyzing the rupture time predictions using the isotropic rupture time prediction model (Eq. (13)), it is necessary to study the isotropic damage prediction (Eq. (14)), which will help facilitate an accurate estimate of critical damage. Work by MacLachlan and Knowles [28] suggests that critical damage is limited by the UTS. Since the UTS is the maximum resistance to fracture, it is a justly assumed criterion. Failure is reached when the net/effective stress (Eq. (7)) is equivalent to the UTS and takes the form

$$\bar{\sigma}_{net} = \frac{\bar{\sigma}}{(1-\omega)} \Rightarrow \omega_f = \frac{UTS - \bar{\sigma}}{UTS} \tag{18}$$

where simplification provides an estimate of critical damage. Table 4 provides a comparison of the isotropic (ISO), MacLachlan–Knowles (MK), and half MK damage predictions. The results demonstrate that the isotropic model (ISO) produces much lower values of critical damage when compared with MK estimates. This inconsistency can be explained. The MacLachlan and Knowles damage formulation directly includes the UTS in the form

$$\frac{d\omega}{dt} = C \times \left(\frac{\bar{\sigma}_{\text{net}}}{\text{UTS} - \bar{\sigma}_{\text{net}}} \right)^{\nu} \tag{19}$$

where C and ν are constants. This provides a method by which failure is assumed when net/effective stress is equal to UTS. The

Table 4 Damage and rupture predictions for DS GTD-111

Matl. orient. α (deg)	Temperature °C	Temperature °F	Stress MPa	Stress ksi	Critical damage, ω_f MK	MK/2	ISO	Experimental rupture time, t_f (h)	Predicted rupture time, t_{rup} (h) ω=1.0	ω=0.25	ω=MK	ω=MK/2
L (0)	649	1200	896	130	0.19	0.10	0.05	465.9	502.9	502.9	502.9	501.2
L (0)	760	1400	408	60	0.63	0.32	0.35	5624.0	5533.2	5173.4	5532.8	5383.0
L (0)	760	1400	613	89	0.45	0.22	0.13	243.6	213.6	210.1	213.6	207.8
T (90)	760	1400	517	75	0.47	0.23	0.13	375.7	338.3	334.7	338.3	333.4
T (90)	760	1400	613	89	0.37	0.19	0.03	42.6	34.1	34.1	34.1	34.1
L (0)	816	1500	455	66	0.54	0.27	0.58	321.5	326.5	244.2	318.6	254.4
T (90)	816	1500	455	66	0.51	0.26	0.06	127.0	110.8	110.8	110.8	110.8
L (0)	871	1600	241	35	0.70	0.35	0.25	2149.0	1952.8	1766.2	1952.7	1894.6
L (0)	871	1600	289	42	0.64	0.32	0.22	672.2	629.1	600.1	629.1	618.9
T (90)	871	1600	241	35	0.71	0.36	0.43	980.2	1158.5	709.6	1139.2	886.2
T (90)	871	1600	289	42	0.65	0.33	0.26	635.3	701.9	628.0	701.8	670.1
L (0)	940	1724	244	35	0.47	0.29	0.31	68.7	65.3	58.9	64.9	61.0
T (90)	940	1724	244	35	0.61	0.26	0.24	62.5	70.5	63.6	70.5	64.6
L (0)	982	1800	124	18	0.35	0.37	0.57	821.3	799.9	566.3	675.0	688.9
L (0)	982	1800	145	21	0.24	0.35	0.33	301.7	278.7	230.8	227.8	258.3

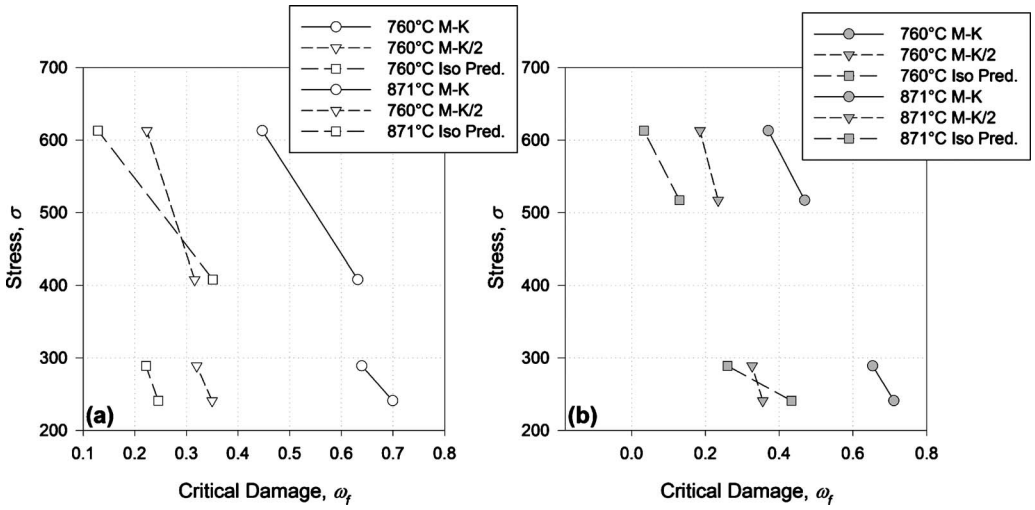

Fig. 11 Stress-damage curves for (*a*) L and (*b*) T orientations at 760°C and 871°C

UTS directly influences not only the point of critical damage but also the rate of damage. The isotropic creep damage formulation does not directly include UTS; thus, the net/effective stress nears infinity at failure, and the damage evolution is not altered. For the purposes of this study, it is found that reducing the MK estimate by half greatly reduced the error between predicted critical damages. This has substantial benefits. Of importance is the relationship between stress and critical damage. Inspection of the applied stress versus critical damage is shown in Fig. 11. It is observed that the ISO critical damage prediction produces a similar trend to the half MK estimates. With additional creep tests, a well defined stress-critical damage curve can be obtained. A function could be created using either prediction method to determine critical damage at a set temperature and orientation.

Based on the critical damage prediction, rupture time predictions using Eq. (13) are performed. Table 4 provides rupture time predictions at various set levels of critical damage. The least conservative estimate is when critical damage is set to unity ($\omega_f = 1.0$). This assumes that failure occurs at a net/effective stress of infinity. Four rupture predictions were nonconservative, with the highest at $1.182t_f$. Next, the critical damage is set to 0.25. This is approximately the average value produced using the isotropic critical damage predictions in Table 4. This provides the second best predictions in terms of conservatism, with only two nonconservative predictions, the highest being $1.0794t_f$. Next, critical damage is set to MK. This generates the results similar to critical damage at unity. Four rupture predictions were nonconservative, with the highest at $1.1622t_f$. Reducing to half MK generates the most conservative predictions with three nonconservative rupture predictions, the highest at $1.0757t_f$.

In most cases where nonconservative estimates were found, the least-squares value at the end of optimization was high. This signifies that additional optimization using a more advanced routine could produce improved constants, resulting in a better estimate of rupture time. In all cases, the rupture time predictions are within a factor of 1.2. When applying a factor of 1.2 or greater, rupture time predictions using a critical damage of unity can be taken as is. Figure 12 provides a visual representation of the rupture time predictions compared with experiment. It shows that reducing the value of critical damage increases the conservatism of rupture time predictions. It also shows predictions with critical damage at unity, although the least conservative, are acceptable.

The following method should be used when attempting to produce the most conservative estimates of rupture time. The MK critical damage (Eq. (18)) should be found using the materials' UTS. The MK estimates should be reduced by half and applied within the rupture time prediction. The advantage of the MK method is that it provides critical damage estimates for the temperature range of available UTS data and at the level of applied stress. The disadvantage, however, is that UTS data are needed for both longitudinal and transverse orientations, necessitating additional mechanical testing.

10 Conclusions

The modified Kachanov–Rabotnov tertiary creep damage material model performed well in modeling the creep response of the DS GTD-111 superalloy. Using the simulated annealing optimization routine produced tertiary creep constants, which accurately predicted the creep deformation at various stress and temperature conditions. The later developed temperature- and stress-dependent regression models were found to accurately and moderately match the optimized tertiary creep constants in the L and T orientations, respectively. Application of the rupture time estimation model shows that it can closely predict rupture times found in experimental data for the L and T orientations. Future work will focus on improving the quality of the T-oriented temperature- and stress-dependent regression formulations via additional mechanical testing.

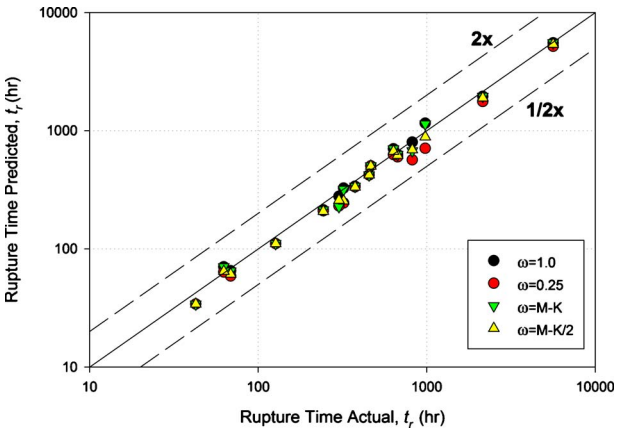

Fig. 12 Rupture time comparison

Acknowledgment

C.M.S. is thankful for the support of the McKnight Doctoral Fellowship through the Florida Education Fund.

References

[1] Daleo, J. A., and Wilson, J. R., 1998, "GTD111 Alloy Material Study," Trans. ASME: J. Eng. Gas Turbines Power, **120**(2), pp. 375–382.
[2] Smallman, R. E., and Bishop, R. J., 1999, *Modern Physical Metallurgy and Materials Engineering: Science, Process, Applications*, Butterworth-Heinemann, Boston, MA.
[3] Ibanez, A. R., 2003, "Modeling Creep Behavior in a Directionally Solidified Nickel Base Superalloy," Ph.D. thesis, Georgia Institute of Technology, Atlanta, GA.
[4] Li, L., 2006, "Repair of Directionally Solidified Superalloy GTD-111 by Laser-Engineered Net Shaping," J. Mater. Sci., **41**(23), pp. 7886–7893.
[5] Schilke, P. W., 2004, *Advanced Gas Turbine Materials and Coatings*, GE Energy, Schenectady, NY.
[6] Schilke, P. W., Foster, A. D., Pepe, J. J., and Beltran, A. M., 1992, "Advanced Materials Propel Progress in Land-Based Gas Turbines," Advanced Materials and Processes, **141**(4), pp. 22–30.
[7] Viswanathan, R., and Scheirer, S. T., 1998, "Materials Advances in Land-Based Gas Turbines," Power-Gen 1998 Conference, Orlando, FL, Dec. 9–11.
[8] Sajjadi, S. A., and Nategh, S., 2001, "A High Temperature Deformation Mechanism Map for the High Performance Ni-Base Superalloy GTD-111," Mater. Sci. Eng., A, **307**(1–2), pp. 158–164.
[9] Hale, J. M., 1994, "Procedure Development for the Repair of GTD-111 Gas Turbine Bucket Material," Eighth Congress and Exposition on Gas Turbines in Cogeneration and Utility, Portland, OR, October, pp. 25–27.
[10] Ibanez, A. R., Srinivasan, V. S., and Saxena, A., 2006, "Creep Deformation and Rupture Behaviour of Directionally-Solidified GTD 111 Superalloy," Fatigue Fract. Eng. Mater. Struct., **29**(12), pp. 1010–1020.
[11] Doi, M., Miki, D., Moritani, T., and Kozakai, T., 2004, "Gamma/Gamma-Prime Microstructure Formed by Phase Separation of Gamma-Prime Precipitates in a Ni-Al-Ti Alloy," Superalloys 2004, TMS, Sept. 19–23, pp. 109–114.
[12] Gordon, A. P., 2006, "Crack Initiation Modeling of a Directionally-Solidified Nickel-Base Superalloy," Ph.D. thesis, Georgia Institute of Technology, Atlanta, GA.
[13] ASTM E-139, "Standard Test Methods for Conducting Creep, Creep-Rupture, and Stress-Rupture Tests of Metallic Materials," No. 03.01, West Conshohocken, PA.
[14] Zuo, M., Chiovelli, S., and Nonaka, Y., 2000, "Fitting Creep-Rupture Life Distribution Using Accelerated Life Testing Data," ASME J. Pressure Vessel Technol., **122**(4), pp. 482–487.
[15] Hyde, T. H., Sun, W., and Tang, A., 1998, "Determination of the Material Constants in Creep Continuum Damage Constitutive Equations," Strain, **34**(3), pp. 83–90.
[16] Hoff, N. J., 1953, "Necking and Rupture of Rods Subjected to Constant Tensile Loads," ASME J. Appl. Mech., **20**(1), pp. 105–108.
[17] Hyde, T. H., Xia, L., and Becker, A. A., 1996, "Prediction of Creep Failure in Aeroengine Materials Under Multiaxial Stress States," Int. J. Mech. Sci., **38**(4), pp. 385–403.
[18] Dorn, J. E., 1955, "Some Fundamental Experiments on High Temperature Creep," J. Mech. Phys. Solids, **3**, pp. 85–116.
[19] Jeong, C. Y., Nam, S. W., and Ginsztler, J., 1999, "Stress Dependence on Stress Relaxation Creep Rate During Tensile Holding Under Creep-Fatigue Interaction in 1Cr-Mo-V Steel," J. Mater. Sci., **34**(11), pp. 2513–2517.
[20] Stewart, C. M., and Gordon, A. P., 2009, "Modeling the Temperature Dependence of Tertiary Creep Damage of a Ni-Based Alloy," ASME J. Pressure Vessel Technol., **131**(5), p. 051406.
[21] McGaw, M. A., 1993, "Cumulative Damage Concepts in Thermomechanical Fatigue," *Thermomechanical Fatigue Behavior of Materials, ASTM STP 1186*, H. Sehitoglu, ed., American Society of Testing and Materials, Philadelphia, PA, pp. 144–156.
[22] Kachanov, L. M., 1967, *The Theory of Creep*, National Lending Library for Science and Technology, Boston Spa, UK.
[23] Rabotnov, Y. N., 1969, *Creep Problems in Structural Members*, North-Holland, Amsterdam.
[24] Johnson, A. E., Henderson, J., and Khan, B., 1962, *Complex-Stress Creep, Relaxation and Fracture of Metallic Alloys*, HMSO, UK.
[25] Hayhurst, D. R., 1983, "On the Role of Continuum Damage on Structural Mechanics," *Engineering Approaches to High Temperature Design*, B. Wilshire and D. R. Owen, eds., Pineridge, Swansea, pp. 85–176.
[26] Murakami, S., and Ohno, N., 1981, "A Continuum Theory of Creep and Creep Damage," *Creep in Structures*, A. R. S. Ponter and D. R. Hayhurst, eds., pp. 422–443.
[27] Stewart, C. M., Gordon, A. P., and Nicholson, D. W., 2009, "Numerical Simulation of Temperature-Dependent, Anisotropic Tertiary Creep Damage," 47th AIAA Aerospace Sciences Meeting Including the New Horizons Forum and Aerospace Exposition, Orlando, FL, Jan. 5–8.
[28] MacLachlan, D. W., and Knowles, D. M., 2000, "Creep-Behavior Modeling of the Single-Crystal Superalloy CMSX-4," Metall. Mater. Trans. A, **31**(5), pp. 1401–1411.
[29] Kouhia, R., Marjamaki, P., and Kivilahti, J., 2005, "On the Implicit Integration of Rate-Dependent Inelastic Constitutive Models," Int. J. Numer. Methods Eng., **62**(13), pp. 1832–1856.
[30] Hogan, E. A., 2009, "An Efficient Method for the Optimization of Viscoplastic Constitutive Model Constants," Honors in the Major Undergraduate thesis, University of Central Florida, Orlando, FL.
[31] Corana, A., Marchesi, M., Martini, C., and Ridella, S., 1987, "Minimizing Multimodal Functions of Continuous Variables With the 'Simulated Annealing' Algorithm," ACM Trans. Math. Softw., **13**(3), pp. 262–280.
[32] Goffe, W. L., Gary, D. F., and Rogers, J., 1993, "Global Optimization of Statistical Functions With Simulated Annealing," J. Econometr., **60**(1/2), pp. 65–100.